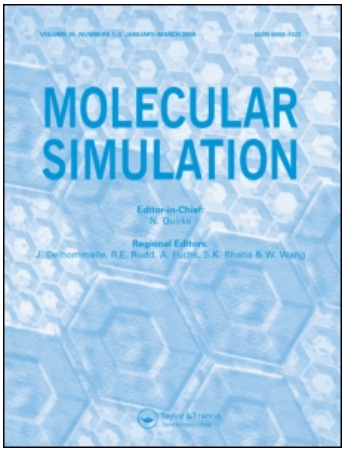

Molecular Simulation
Publication details, including instructions for authors and subscription information:
http://www.informaworld.com/smpp/title~content=t713644482

Non-equilibrium molecular dynamics study of nanoscale thermal contact resistance

Heng Xiang[a]; Pei-Xue Jiang[a]; Qi-Xin Liu[a]
[a] Key Laboratory for Thermal Science and Power Engineering of Ministry of Education, Department of Thermal Engineering, Tsinghua University, Beijing, P. R. China

To cite this Article Xiang, Heng , Jiang, Pei-Xue and Liu, Qi-Xin(2008) 'Non-equilibrium molecular dynamics study of nanoscale thermal contact resistance', Molecular Simulation, 34: 7, 679 — 687
To link to this Article: DOI: 10.1080/08927020802101700
URL: http://dx.doi.org/10.1080/08927020802101700

Molecular Simulation
Vol. 34, No. 7, June 2008, 679–687

Taylor & Francis
Taylor & Francis Group

Non-equilibrium molecular dynamics study of nanoscale thermal contact resistance

Heng Xiang, Pei-Xue Jiang* and Qi-Xin Liu

Key Laboratory for Thermal Science and Power Engineering of Ministry of Education, Department of Thermal Engineering, Tsinghua University, Beijing, P. R. China

(*Received 25 October 2007; final version received 27 March 2008*)

Interfaces play an important role in microscale and nanoscale heat transfer processes with molecular dynamics (MD) simulations often used to study these interfacial phenomena. In this study, two models were used to simulate thermal conduction across micro contact points and the thermal contact resistance using non-equilibrium molecular dynamics simulations with consideration of the near field radiation. When the ratio of the length of the micro contact to the length of the conduction region is less than 0.125, the influence of the near field radiation should be considered; but when the ratio is larger than 0.2, it can be neglected. When the computational domain sizes are $8.50 \times 10.62 \times 8.50$ nm and $10.62 \times 10.62 \times 10.62$ nm, the MD results show that the thermal contact resistance exponentially increases with decreasing area of the micro contact point and increases with increasing micro contact layer thickness. The MD thermal contact resistances in nanoscale are much larger than that of the classical thermal analysis since the material thermal conductivity reduction is ignored in the classical model. The results also show that material defects increase the thermal resistance.

Keywords: thermal contact resistance; molecular dynamics; micro contact; near field radiation

1. Introduction

The continuing demand for integration and microminiaturisation is pushing the evolution of material science and technology. With the development of improved synthesis and fabrication technologies, the characteristic lengths of electronic and mechanical devices are approaching nanometer scales which increase the power dissipation per unit area. Scientific understanding of nanoscale thermal transport mechanisms can help improve device thermal management. Besides, the material thermal conductivity, the interface structure also plays an important role in microscale and nanoscale heat transfer.

When heat flows across an interface between two different materials, there will in general be a macroscopic temperature discontinuity at the interface. The thermal resistance which occurs at the interface when heat flows from a solid into liquid helium was originally called Kapitza resistance with this name later applied to any heat flows from a solid into a liquid or into another solid. The two current theoretical models of the interfacial resistance for phonon-mediated thermal transport are the acoustic mismatched model (AMM; [1]) and the diffuse mismatched model (DMM; [2]). Both models attempt to describe how and why phonons are interrupted at interfaces. The difference between these two models is that the AMM assumes specular interactions at a smooth interface while the DMM assumes diffuse scattering at a rough interface. Another powerful tool to study these interfacial phenomena is the molecular dynamics (MD) method. Maiti et al. [3] used non-equilibrium molecular dynamics (NEMD) simulations to calculate the Kapitza resistance of Si grain boundaries and to demonstrate that local equilibrium can be achieved in small numbers of atomic layers over long simulation runs. Volz et al. [4] used equilibrium molecular dynamics simulations to investigate the interfacial effects in silicon–germanium superlattices and discovered that the strain greatly affects the overall thermal conductivity of the superlattices. Abramson et al. [5] carried out NEMD simulations to study how various factors affect the thermal conductivity of bi-material thin films containing one or more solid–solid interfaces. Twu and Ho [6] analysed the impact of interface disorder on the Kapitza resistance. Schelling et al. [7] computed the Kapitza resistance of three twisted grain boundaries in silicon using the NEMD method. Stevens et al. [8] utilised NEMD to study the Kapitza resistance between two face-centred cubic (FCC) structured Lennard-Jones (L-J) crystals. Chen et al. [9] used NEMD to calculate the lattice thermal conductivities of Ar and Kr/Ar nanostructures to study the effects of interface scattering, boundary scattering and elastic strain on the lattice thermal conductivity. Choi and Maruyama [10] investigated the thermal boundary resistance using NEMD

*Corresponding author. Email: jiangpx@tsinghua.edu.cn

ISSN 0892-7022 print/ISSN 1029-0435 online

DOI: 10.1080/08927020802101700
http://www.informaworld.com

and found excellent agreement with the results of the updated C–M model.

However, all of above investigations only considered the thermal resistance resulting from 'perfect' contact between two dissimilar materials which some people call the thermal boundary resistance. Actually, the interface effects on the thermal transport are due to the different properties of the dissimilar materials and the contact geometry. Many nanoscale studies have analysed the effect of the dissimilar material properties, but few have focused on the effect of the geometry. Liang and Sun [11] used a model with a staggered interface between two materials to study the interface influence using the NEMD method. Hegedus and Abramson [12] used NEMD to study the thermal transport in heterogeneous thin film systems, including layered systems and nanocomposites. Liang and Sun [11] and Hegedus and Abramson [12] both sought to understand the multi-layered thin films used in microelectronic multi-layer packages. Except for the multi-layered thin films, 'imperfect' contact normally occurs between surfaces, for example, in porous media. Nanoscale porous media have a very high specific surface area and are widely used for catalytic reactions. Nanoscale porous media are made of nanoparticles with 'imperfect' contact between the particles which affects the heat transport.

The thermal resistance at an interface between two imperfect surfaces is usually referred to as the thermal contact resistance. Thermal energy is transferred between the contacting bodies by: (i) conduction at the micro contact points, (ii) conduction through the interstitial fluid in the gap between the contacting solids and (iii) thermal radiation across the gap [13]. This study assumed no fluid in the limited interstitial spaces, so there is no conduction through the interstitial fluid. Generally, the radiation heat transfer is quite small and can be neglected for surface temperatures up to 700 K [13]. However, some recent research has shown that the near field radiation intensity will be pronounced in nanoscale systems [14]. Therefore, this study included the effect of the near field radiation. This paper describes two models for simulating conduction through the interface contact points to calculate the thermal contact resistance using NEMD simulations.

2. Physical model and MD simulation method

Figure 1, shows a scanning electron microscope (SEM) photograph of a porous media made of sintered copper particles. The figure shows the actual micro scale contact areas between particles. There are many nanoscale size gaps between particles.

The nanoscale thermal contact resistance was studied using the MD method by replacing the real contact

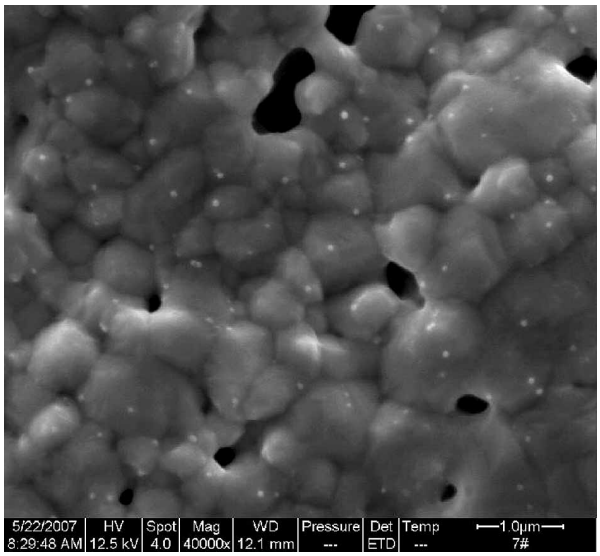

Figure 1. SEM photograph of a sintered porous media.

geometry by an ideal geometry. The material contact was simplified to the model shown in Figure 2 with one representative part selected for modelling. The four blank squares simulate gaps between the contacting surfaces. The region marked by the dashed line was used for the analysis.

Two models were constructed for the MD simulations to investigate the thermal contact resistance. Figure 3, shows the model I which was divided into six segments with three sets of stationary atoms, a cold bath, a hot bath and an inner segment with regular atoms. The stationary atoms at each end of the model were used to keep the simulated material from evaporating and escaping into the vacuum. Their positions were never updated after initialisation, but their presence was considered during the force calculations. The regions with the hot and cold atoms were defined as temperature baths to control the temperature via velocity rescaling, so a temperature gradient was imposed along the length of the lattice (y-axis). The region with the regular atoms was the conduction region, with a selected layer of atoms in the middle of the conduction region set as stationary atoms to simulate gaps with only a small contact region between regular atoms in the centre. Periodic boundary

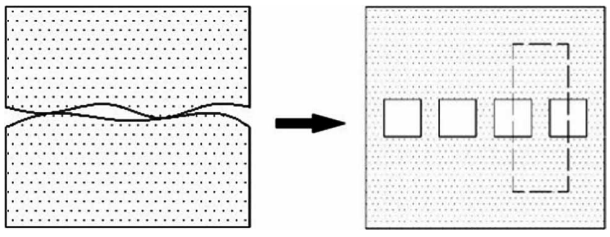

Figure 2. Physical model of the thermal contact resistance.

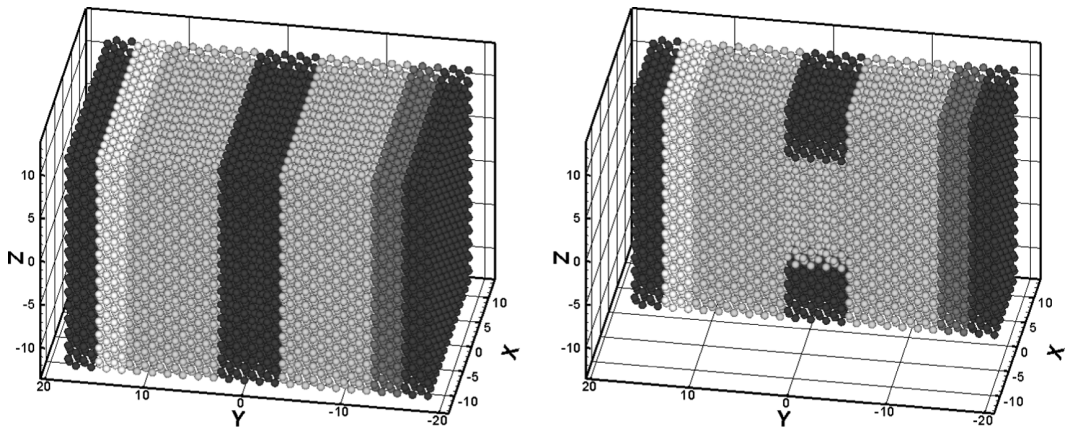

Figure 3. The model I for the MD simulations. The white and dark-gray atoms belong to the hot and cold baths, the light-gray atoms belong to the conduction region and the black atoms are stationary atoms. The right figure is a central plane sectional view of the left figure.

conditions were used in the x- and z-directions. The coordinate system origin was set at the centre of the model.

Figure 4, shows the model II used for the MD simulations. The model was divided into five segments with two sets of stationary atoms, a cold bath, a hot bath and an inner segment with regular atoms. The difference between these two models is that the stationary atoms in the middle of the conduction region in the first model were removed in the second model to create a 'vacuum' for the gaps in the materials.

The thermal contact resistance problem is complicated because many factors affect the thermal resistance [13]. In this study, only the size of the contact region which is surrounded by stationary atoms or a vacuum was varied to simulate various contact geometries and to investigate their effects on the thermal contact resistance.

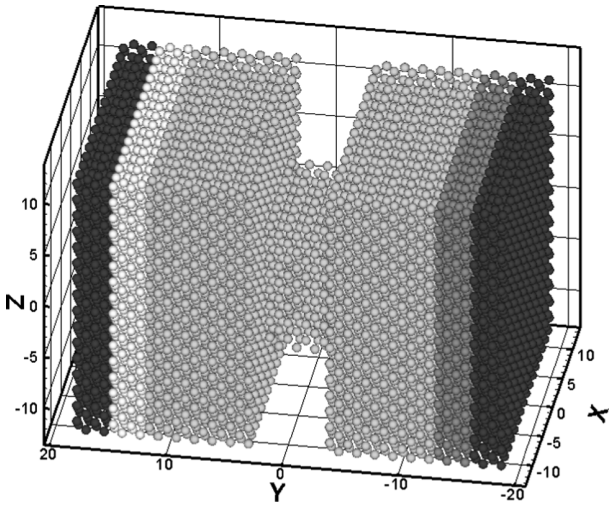

Figure 4. The model II for the MD simulations. The white and dark-gray atoms belong to the hot and cold baths, the light-gray atoms belong to the conduction region and the black atoms are stationary.

For all cases, the overall thermal resistance of the entire structure, R_S, was analysed using a simple series resistance calculation involving the thin film thermal resistance, R_F and the contact thermal resistance, R_C, resulting from the 'disturbance'. That is

$$R_S = R_F + R_C. \tag{1}$$

According to the thermal resistance definition, $R = \Delta T/Q$ and R_S is given by

$$R_S = \frac{2n\Delta t\Delta T}{\Delta E_{k,\text{in}} + \Delta E_{k,\text{out}}}, \tag{2}$$

where $\Delta E_{k,\text{in}}$ is the heat inflow to the hot region,

$$\Delta E_{k,\text{in}} = \frac{1}{2}\sum_{j=1}^{n_{TC}}\sum_{i=1}^{N_{hot}} m\left(v_{i,\text{new}}^2 - v_{i,\text{old}}^2\right),$$

and $\Delta E_{k,\text{out}}$ is the heat outflow from the cold region,

$$\Delta E_{k,\text{out}} = \frac{1}{2}\sum_{j=1}^{n_{TC}}\sum_{i=1}^{N_{cold}} m\left(v_{i,\text{old}}^2 - v_{i,\text{new}}^2\right),$$

where N_{hot} and N_{cold} are the number of molecules in the hot and cold temperature control layers and n_{TC} is the total number of velocity scalings over the period of one run. Δt is the time interval, n is the total number of simulation steps and ΔT is the temperature difference between the cold and hot ends.

An instantaneous temperature was calculated from the planar average of the kinetic energy of the atoms

in each x–z-plane such that

$$T_{\mathrm{MD}} = \frac{\left\langle \sum_{i=1}^{N} m_i v_i \right\rangle}{3Nk_{\mathrm{B}}}, \tag{3}$$

where $\langle\rangle$ denotes statistical averaging over all of the simulation time, m is the mass, v the atom speed, N is the total number of atoms in the specific x–z-plane and k_{B} is Boltzmann's constant. Equation (3) is a classical formula valid only at very high temperatures ($T \gg T_{\mathrm{Debye}}$), where $T_{\mathrm{Debye}} = 92\,\mathrm{K}$ is the Debye temperature for argon. In this case, the system average temperature ($T = 25\,\mathrm{K}$) is lower than the Debye temperature, so a quantum correction must be applied. Because the system energy from classical statistics should be equal to that from the quantum description

$$3Nk_{\mathrm{B}}T_{\mathrm{MD}} = \int_0^{v_{\mathrm{D}}} D(v)n(v,T)\hbar v \mathrm{d}v, \tag{4}$$

where the right-hand side represents the total phonon energy in the system, D is the density of states, v is the phonon frequency and n defines the phonon occupation number. Equation (4) can then be used to deduce the real system temperature T appearing in function n. Since ΔT is involved in Equation (2), R_{S} should be rescaled by the $\Delta T/\Delta T_{\mathrm{MD}}$ obtained from Equation (4). Volz et al. [4], demonstrated that the quantum correction changes the absolute value of the temperature, but the relative value is not obviously affected when the temperature is away from zero. Thus, the quantum correction does not have a significant influence on the results for R_{S} and ΔT_{MD} can be used directly in Equation (2).

In the simulations, the desired hot and cold bath temperatures were maintained by periodically adjusting the atomic velocities.

$$v_{i,\mathrm{new}} = v_{i,\mathrm{old}}\sqrt{T_{\mathrm{d}}/T_i}, \tag{5}$$

where T_{d} is the desired temperature and T_i is the instantaneous temperature. Note that Equation (5) does allow for some net change in momentum during a single time step, but the net momentum change vanishes because of averaging over an adequate time period. In this study, the velocities were adjusted every 10 time steps.

A true representation of the intermolecular potential is critical in these MD simulations, so all the simulations used argon as the material due to the availability of a good intermolecular potential for argon. All the atomic interactions were described by the widely accepted L-J 12-6 potential model:

$$u(r) = 4\varepsilon[(\sigma/r)^{12} - (\sigma/r)^{6}], \tag{6}$$

where r is the distance between two atoms, ε is the well depth parameter and σ is the equilibrium separation parameter. The cut-off radius, r_{c}, was set to 2.5 σ. The force experienced by an atom due to the presence of another atom is simply the first derivative of Equation (6). Newton's equations of motion is used to relate the force and the atom acceleration The commonly employed velocity Verlet algorithm [15] was used with the acceleration expressed in terms of velocity, position and time and the solution then marched in time. To increase the precision of the computations, the standard LJ non-dimensionalisations were used for the parameters in the simulations [15]. A revised version of the Large-scale Atomic/Molecular Massively Parallel Simulator (LAMMPS) program [16] was used for the simulations.

The condition was similar to those in Chantrenne and Barrat's paper [17]. The critical input parameters for all the simulations are listed in Table 1.

The time step must be carefully chosen in MD simulations. If the time step is too small, the simulations will take too long to reach steady state. If the time step is too large, the details of the atomic movements will be lost and the phonon behaviour will not be accurately captured. In all these simulations, the time step was 1×10^{-14} s (10 fs), which reduces the computer time to a reasonable level while providing reasonable detail of the atom and phonon behaviour. A few simulations of the nanoscale thermal conduction were conducted with different time steps to confirm that 10 fs was sufficiently small to give accurate results, with the results in Table 2 showing that the results are accurate for 10 fs. To get reliable results, the simulations were run 5×10^5 steps, which is a total of 5 ns. After the heating and cooling were initiated, the system was allowed to reach steady state conditions in the first 1×10^5 steps, with the temperature distribution and heat flux calculated during the next 4×10^5 steps. The relative energy error over the entire simulation period did not exceed 0.05% once the system reached steady state.

The dimension parameters used in the simulations are listed in Table 3. The corresponding computational domain sizes were $8.50 \times 10.62 \times 8.50$ nm and $10.62 \times 10.62 \times 10.62$ nm (x–z-directions). The two domains included 20,480 and 32,000 molecules. To facilitate the data reduction, two dimensionless

Table 1. Parameters used in all simulations.

Parameter	Value
LJ well depth	1.67×10^{-21} J
LJ equilibrium separation	3.4×10^{-10} m
Boltzmann's constant	1.38×10^{-23} J/K
Argon atomic mass	6.64×10^{-26} kg
Lattice constant	5.28×10^{-10} m
Time step	1×10^{-14} s
Hot region temperature	27 K ($T^* = 0.2254$)
Cold region temperature	23 K ($T^* = 0.1920$)

Table 2. Predicted overall thermal resistances for various time steps.

Time step (fs)	Normalised value of R_S
10	1
5	0.998481
1	0.994173

Table 3. Geometric parameters.

Parameter	Value
Fixed atom wall thickness	2 unit cells
Hot bath thickness	2 unit cells
Cold bath thickness	2 unit cells
Regular region thickness	16 unit cells
Cross-section size ($x-z$-directions)	16 × 16 and 20 × 20 unit cells

parameters, $c_1 = S_a/S_b$ and $c_2 = L_a/L_b$, were introduced to describe the area and thickness of the micro contact region, where S_a and L_a are the area and thickness of the contact region and S_b and L_b are the area and thickness of the regular region as illustrated in Figure 5. The size of the contact region was varied to give different contact geometries to investigate the thermal contact resistance variations with the contact geometry.

3. Results and discussion

Figures 6 and 7 show representative snapshots of the micro contact region whose size was 10 × 6 × 10 cell lengths ($x-z$-directions) in models I and II, including front and side views, at step 5×10^5. The outer squares and rectangles in Figures 6 and 7 indicate the sampling region, while the inner squares indicate the initial position of the regular atoms in the micro contact region. The atom colours vary from blue to red to indicate atomic kinetic energies from low to high. Figure 6 for model I

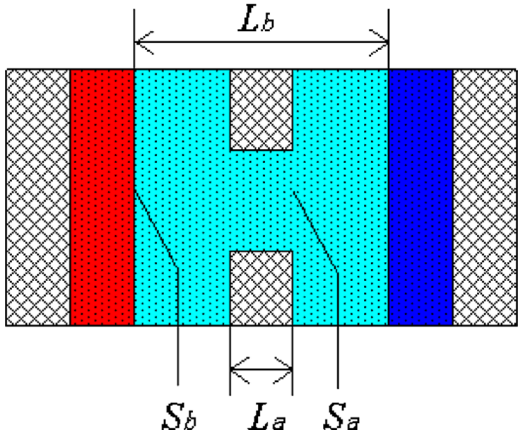

Figure 5. Diagram of S_a, S_b, L_a and L_b.

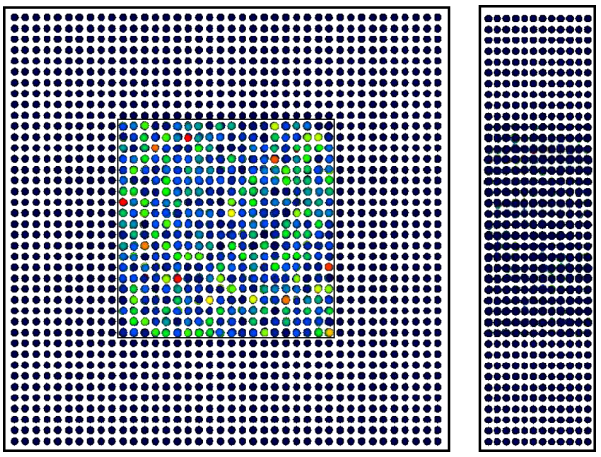

Figure 6. Snapshot of the micro contact region in model I.

shows that the atoms maintain the initial FCC structure with few changing positions. However, in Figure 7 for model II, the situation is different with the initial structure changed some what with some atoms even leaving their initial positions and escaping into the vacuum. This phenomenon is equivalent to the interatomic distance change and some partial inflation occurs.

The simulation region was divided into many layers having one unit cell thickness in the y-direction with each layer being a plane, with 1024 or 1600 atoms per layers. Maiti et al. [3], showed that these numbers of atoms are adequate to calculate the local temperature over long simulation runs. The temperature distribution along the y-direction was obtained by summing the kinetic energies of the atoms in each plane. Figure 8, shows representative dimensionless temperature distributions in the y-direction for models I and II, for the micro contact region of 10 × 6 × 10 cell lengths ($x-z$-directions) and the domain region of 20 × 16 × 20 cell lengths ($x-z$-directions).

The results in Figure 8 show that the temperature distributions predicted by model I and model II are similar with some small differences. The temperature gradients in both models increase significantly in the contact region which will increase the heat flux. The heat fluxes increase because the conduction cross-sections both shrink in two models in the contact regions. The slight difference between the results for the two models is that the temperature gradients in the two models are slightly different in the contact region and the temperature jumps in the two models are also slightly different at the ends of the contact region. The temperature distribution along the y-direction indicates the local heat transfer ability. If the temperature gradient is high, the local heat transfer rate is relatively low. Therefore, the results in Figure 8 indicate that the local heat transfer rate in the contact region of model II is appreciably lower than that of model I. These differences

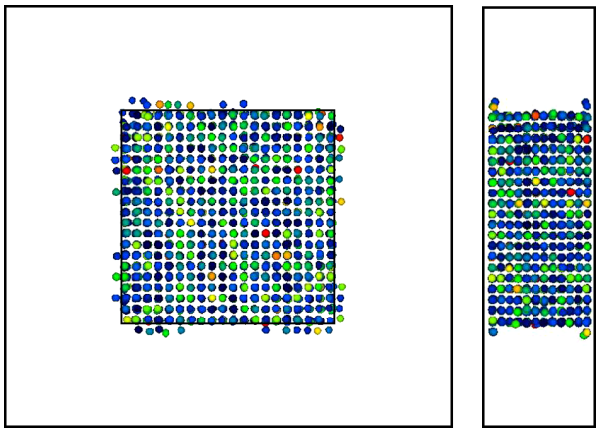

Figure 7. Snapshot of the micro contact region in model II.

arise from the different models used in model I and model II, with the partial inflation in model II creating more thermal resistance which reduces the local heat transfer rate.

Some recent research has shown that the near field radiation intensity is pronounced in nanoscale systems [14]. Thus, if the gaps between the materials are thin enough, the heat flux will become very large and the heat transfer due to the near field radiation will be a large proportion of the total heat transfer in the system. If the near field radiation is neglected, the heat flux will be reduced and the thermal conductivity will be underestimated. The heat flux between two parallel planes [14] can be expressed as:

$$Q = \int_0^\infty [Q_{12}(\omega) + Q_{21}(\omega)]\,\mathrm{d}\omega, \tag{7}$$

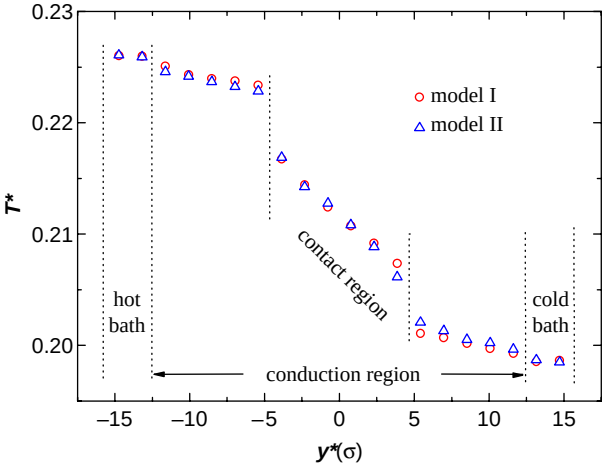

Figure 8. Dimensionless temperature distribution along the y-direction.

where Q_{12} is the monochromatic radiation intensity and ω is the frequency. Q_{12} for a dielectric plane is

$$Q_{12} = \frac{hck^3}{8\pi^3[\exp(hkc/2\pi k_B T_1) - 1]}\left[\frac{0.6806}{\pi^2 y^2} + \frac{m(m+1)}{y^2}\right], \tag{8}$$

where h is Planck's constant, c is the speed of light, k is the wave number, T is the surface temperature, y is a nondimensional number and $m = \mathrm{int}\,(y)$. From Equations (7) and (8), when c_2 is equal to 0.125 (the gap thickness is 1.06 nm) as in this study, the heat flux due to the near field radiation will approach $7.0 \times 10^6\,\mathrm{W/m^2}$. Thus, considering the area ratio for radiation and conduction, the maximum ratio of the near field radiation and the conduction heat fluxes is 40%. When c_2 is larger than 0.2, the influence of the near field radiation on the total heat flux becomes insignificant (less than 2%). Therefore, the near field radiation was included in the analyses when c_2 was less than 0.2.

From the classical thermal analysis of a heat source in a half-space, the spreading resistances for isothermal and isoflux boundary conditions are $R_{s,\,\mathrm{isothermal}} = 1/4$ and $R_{s,\,\mathrm{isoflux}} = 8/3\pi^2$ ka [13]. Real contact geometries have many micro contact points with various sizes, so a constriction parameter and correlation were developed to account for the interference between neighboring micro contact points. When two identical constriction and spreading resistance are in series, Roess [18] suggested the expression $R = \psi(\varepsilon)/2k_s a$, where, $k_s = 2k_1k_2/(k_1 + k_2)$ is the harmonic mean of the thermal conductivities and ε is the constriction parameter. In the next discussion, Gibson's factor correlation [13] was selected for the classical thermal spreading resistance.

Since, the absolute values of the nanoscale thermal contact resistance are not intuitive, the ratio of R_C to R_F is introduced to describe the results. Though the thin film thermal conductivity varies with the film thickness and the film average temperature, the film thickness and the film average temperature are equal in the corresponding thermal contact resistance models, so R_F can be used as a reference for the variations of R_C. For the same simulation conditions and the 16 unit cell thickness, the film thermal conductivity simulation result was about 42 (in LJ units). This result agrees well with that in Chantrenne and Barrat [17] whose boundary condition was free surfaces with dead atoms.

The variations of the ratio of R_C to R_F with c_1 and c_2 are illustrated in Figures 9 and 10. Figure 9, shows that although the computational domain sizes and the computation models differed, the variations of the ratio of R_C to R_F are similar with the ratio decreasing at nearly same rate with increasing c_1 for different domain sizes in the same model when c_2 is held constant with little difference between the results of models I and II.

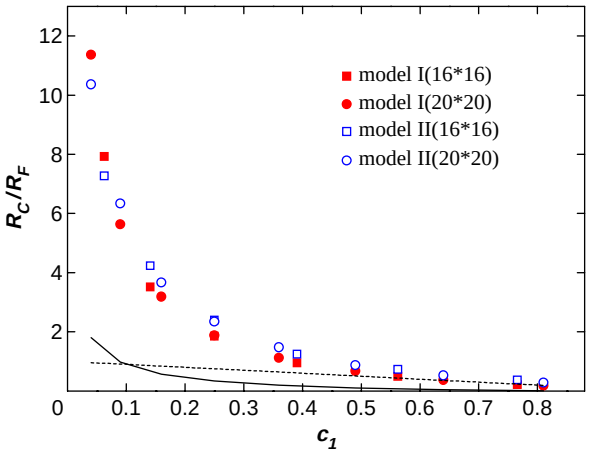

Figure 9. Variation of thermal contact resistance with c_1 ($c_2 = 0.125$) for domain cross-sections (x–z-directions) of 16 × 16 and 20 × 20 unit cells. The dashed line is the value of $(1 - c_1)$. The solid line is the result of the classical thermal analysis [13].

The results also show that the thermal contact resistance increases exponentially with decreasing c_1 and is very large when c_1 is quite small. When c_1 is less than 0.1, the ratio of R_C to R_F exceeds 5. The dashed line in Figure 9 is the value of $(1 - c_1)$ which is the ratio of the 'disturbance' area to the regular region area (domain cross-sectional area). When c_1 is larger than 0.5, the ratio of R_C to R_F is close to $(1 - c_1)$, but when c_1 is smaller than 0.5, the ratio of R_C to R_F is much larger than $(1 - c_1)$. Thus, the heat transfer rate decrease is not linearly related to the contact region area decrease, especially when the contact region area is smaller than half of the system area. The solid line in Figure 9 is the result of the classical thermal analysis [13] which are much smaller than the MD simulation results. Figure 10, shows that the ratio of R_C to R_F increased uniformly with

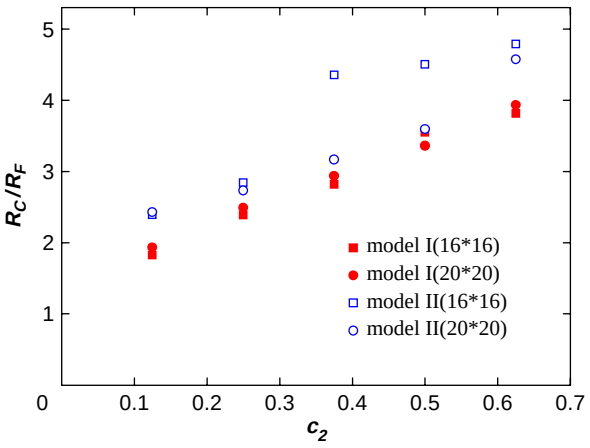

Figure 10. Variation of thermal contact resistance with c_2 ($c_1 = 0.25$).

increasing c_2 when c_1 was held constant. In model I, the ratio increases at nearly the same rate for different domain sizes, but in model II, there are some fluctuations in rate of increase.

According to kinetic theory, the thermal conductivity of a dielectric material is given by

$$k = \frac{1}{3} c_v v l, \tag{9}$$

where c_v is the specific heat capacity of a phonon, v is the phonon velocity in a material and l is the phonon mean free path between phonon scattering events. When the material and the state point are selected, there is little variation of c_v and v and k is proportional to the phonon mean free path.

The phonon transfer process can be described as in Figure 11. The empty region represents the conduction region (regular atom region), the cross-hatched regions represent the gaps, the solid lines with arrows represent the phonon paths and the dashed lines with arrows represent the phonon paths after interactions with the boundary or partial inflation. The boundaries cause specular and scattered reflections (such as approaching the fixed atom wall), diffuse scattering caused by partial inflation (the partial inflation is indicated by circles), constriction along the phonon path, etc. The reflection, scattering and constriction can all intensify the phonon collisions and reduce the phonon mean free path. From Equation (9), when the phonon mean free path decreases, the material thermal conductivity will decrease. In Figure 9, the ratio of R_C to R_F increases with decreasing

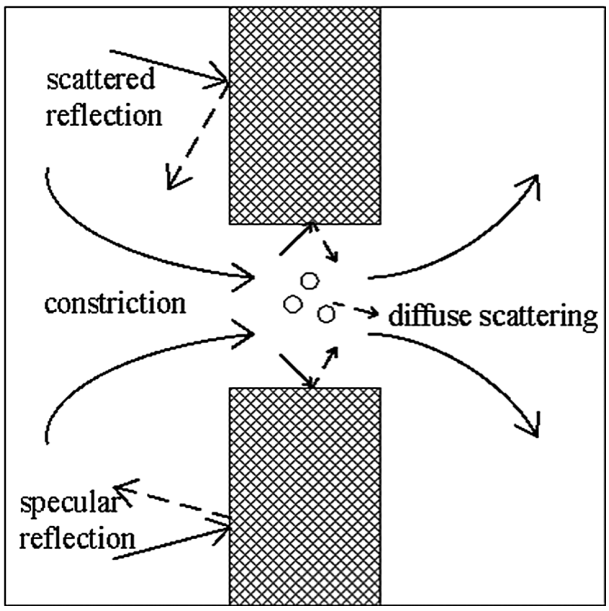

Figure 11. Sketch of phonon transfer.

c_1. A reduced c_1 will: (i) increase the blocked area and intensify the phonon reflections on the obstacles, and (ii) restrict the phonon paths. These two factors will both increase the phonon collisions. The results of the classical thermal analysis are much smaller than the MD simulation results. Both macro and classical thermal analyse consider only the geometric effect on the heat flux without considering changes of the material thermal conductivity caused by phonon reflection, scattering and constriction. When the contact area is large, the thermal conductivity reduction is small and can be ignored, but in nanoscale systems, the change in the heat flux caused by the thermal conductivity reduction will be a large proportion of the overall change and should be considered. In Figure 10, the ratio of R_C to R_F increases with increasing c_2 because the phonon collision probability increases when the phonons are transmitted over longer distances in the narrow channel. In addition, the results of model II in Figure 10 are all larger than the results of model I due to the partial inflation phenomenon in model II, so the atomic vibrations are not transmitted as in a normal material which is equivalent to the phonon being scattered and the mean free path being more reduced. Since the partial inflation is stochastic, the mean free path reduction brought about by the partial inflation will not be uniform, so the thermal contact resistance in model II does not increase at the same rate in Figure 10 as that in model I. The phonon transmission will not be affected by the partial inflation until the inflation reaches some level. Thus, the thermal contact resistance of model II is not larger than that of model I when c_1 is less than 0.1.

From a macroscopic viewpoint, when two slabs contact, the thermal contact resistance decreases with increasing pressure on the slabs. The mechanisms are that when the pressure is increased, material deformation increases the micro contact area which increases c_1 and reduces the thermal contact resistance. Also, when the pressure is increased, the material deformation reduces the micro contact region length, so c_2 and thermal contact resistance decrease.

The actual physical situation described by these two micro thermal contact resistance models is related to the boundary conditions. The fixed atoms in the regions embedded in the conduction region correspond to a vacuum in a macro scale model since the fixed atoms prevent the regular atoms from entering some regions, which is quite similar to a vacuum. When a disturbance is due to a 'vacuum', the corresponding actual physical system is a material defect, so a vacuum disturbance causes some changes in the atomic arrangement which is similar to a material with defects. The results in Figures 9 and 10 show that in most cases the ratio of R_C to R_F for model II is larger than that for model I. This means that the material defects increase the thermal resistance, which is consistent with previous studies [19].

4. Summary and conclusions

From a microscopic viewpoint, heat flows across a contact interface by conduction at the micro contact points, conduction through the interstitial fluid in the gap between the contacting solids and thermal radiation across the gap. This study analysed the conduction across the micro contact regions and the thermal radiation. Two models were constructed to simulate the conduction at the micro contact points by NEMD simulations with two types of obstacles employed to represent the gap between two imperfect surfaces. One obstacle was represented by fixed atoms with the other being a vacuum. The thermal contact resistance variations with the contact geometry were investigated by changing the size parameters of the contact regions in the models. The L-J 12-6 potential model was used to describe the interactions between atoms with a revised version of the LAMMPS program used for the simulations. The near field radiation was also considered. The computational results show that when c_2 is equal to 0.125, the ratio the near field radiation and conduction heat fluxes is a maximum equal to 40%, so the NEMD simulation results were corrected. However, when c_2 is larger than 0.2, the near field radiation influence on the total heat flux becomes insignificant (less than 2%) and can be neglected.

When the computational domain sizes are $8.50 \times 10.62 \times 8.50$ nm and $10.62 \times 10.62 \times 10.62$ nm, the simulation results show that the ratio of R_C to R_F increases exponentially with decreasing micro contact area and increases with increasing micro contact layer thickness. This conclusion helps to explain the macro thermal resistance increases with increasing pressure since the material deformation caused by the increasing pressure will increase the micro contact area and reduce the micro contact region length, so c_1 increases and c_2 decreases; therefore, the thermal contact resistance decreases. The MD results are much larger than that of the classical thermal analysis since the effects of phonon reflection, scattering and constriction on the material thermal conductivity reduction are neglected in the classical thermal analysis. The results also show that material defects will increase the thermal resistance. In these models, the disturbances due to the fixed atoms embedded in the conduction region correspond to a vacuum in the macro world with the 'vacuum' disturbances corresponding to defects in the material.

Acknowledgements

This project was supported by the National Natural Science Foundation of China (No. 50676047) and the Tsinghua Basic Research Foundation (No. JCpy2005049). The computations were supported by the THPCC.

References

[1] I.M. Khalatnikov and I.N. Adamenkoz, *Theory of the Kapitza temperature discontinuity at a solid body–liquid helium boundary*, Soviet Phys. JETP 36 (1973), pp. 361–387.

[2] E.T. Swartz and R.O. Pohl, *Thermal resistance at interface*, Appl. Phys. Lett. 51 (1987), pp. 2200–2202.

[3] A. Maiti, G.D. Mahan, and S.T. Pantelides, *Dynamical simulations of nonequilibrium processes – heat flow and the Kapitza resistance across grain boundaries*, Solid State Commun. 102 (1997), pp. 517–521.

[4] S. Volz, J.B. Saulnier, G. Chen, and P. Beauchamp, *Computation of thermal conductivity of Si/Ge superlattices by molecular dynamics techniques*, Microelectron. J. 31 (2000), pp. 815–819.

[5] A.R. Abramson, C.-L. Tien, and A. Majumdar, *Interface and strain effects on the thermal conductivity of heterostructures: A molecular dynamics study*, J. Heat Transfer ASME 124 (2002), pp. 963–970.

[6] W.C.-J. Twu and W.J.-R. Ho, *Molecular-dynamics study of energy flow and the Kapitza conductance across an interface with imperfection formed by two dielectric thin films*, Phys. Rev. B, Condens. Matter Mater. Phys. (USA) 67 (2003), pp. 205421–205428.

[7] P.K. Schelling, S.R. Phillpot, and P. Keblinski, *Kapitza conductance and phonon scattering at grain boundaries by simulation*, J. Appl. Phys. 95 (2004), pp. 6082–6091.

[8] R.J. Stevens, P.M. Norris, and L.V. Zhigilei, *Molecular-dynamics study of thermal boundary resistance: Evidence of strong inelastic scattering transport channels*, Am. Soc. Mech. Eng. Electron. Photon. Packag. EPP 4 (2004), pp. 37–46.

[9] Y. Chen, D. Li, J. Yang, Y. Wu, J.R. Lukes, and A. Majumdar, *Molecular dynamics study of the lattice thermal conductivity of Kr/Ar superlattice nanowires*, Physica B: Condens. Matter 349 (2004), pp. 270–280.

[10] S.-H. Choi and S. Maruyama, *Thermal boundary resistance at an epitaxially perfect interface of thin films*, Int. J. Therm. Sci. 44 (2005), pp. 547–558.

[11] X.-G. Liang and L. Sun, *Interface structure influence on thermal resistance across double-layered nanofilms*, Microscale Thermophys. Eng. 9 (2005), pp. 295–304.

[12] P.J. Hegedus and A.R. Abramson, *A molecular dynamics study of interfacial thermal transport in heterogeneous systems*, Int. Heat Mass Transfer 49 (2006), pp. 4921–4931.

[13] M. Bahrami, J.R. Culham, M.M. Yananovich, and G.E. Schneider, *Review of thermal joint resistance models for nonconforming rough surfaces*, Appl. Mech. Rev. 59 (2006), pp. 1–12.

[14] M.H. Han and X.G. Liang, *Comparison of heat conduction and radiation of nano-size gas gaps*, in *First International Conference on Microchannels and Minichannels*, Rochester, NewYork, 2003.

[15] M.P. Allen and D.J. Tildesley, *Computer Simulation of Liquids*, Clarendon Press, Oxford, 1987.

[16] S. Plimpton, *Fast parallel algorithms for short-range molecular dynamics*, J. Comput. Phys. 117 (1995), pp. 1–19.

[17] P. Chantrenne and J.-L. Barrat, *Finite size effects in determination of thermal conductivities: Comparing molecular dynamics results with simple models*, J. Heat Transfer ASME 126 (2004), pp. 577–585.

[18] L.C. Roess, *Theory of Spreading Conductance*, Beacon Laboratories of Texas, Beacon, NY, Appendix A (unpublished paper) 1950.

[19] J.R. Lukes and C.L. Tien, *Molecular dynamics simulation of thermal conduction in nanoporous thin films*, Microscale Thermophys. Eng. 8 (2004), pp. 341–359.